We are IntechOpen, the world's leading publisher of Open Access books Built by scientists, for scientists

4,800
Open access books available

122,000
International authors and editors

135M
Downloads

Our authors are among the

154
Countries delivered to

TOP 1%
most cited scientists

12.2%
Contributors from top 500 universities

WEB OF SCIENCE™

Selection of our books indexed in the Book Citation Index in Web of Science™ Core Collection (BKCI)

Interested in publishing with us?
Contact book.department@intechopen.com

Numbers displayed above are based on latest data collected.
For more information visit www.intechopen.com

Chapter 5

Aerosols Monitored by Satellite Remote Sensing

Zhihua Mao, Xueliang Deng, Peng Chen,
Bangyi Tao, Guanying Yang, Yanfeng Huo and
Qiankun Zhu

Additional information is available at the end of the chapter

http://dx.doi.org/10.5772/65284

Abstract

Aerosols, small particles suspended in the atmosphere, affect the air quality and climate change. Their distributions can be monitored by satellite remote sensing. Many images of aerosol properties are available from websites as the by-products of the atmospheric correction of the satellite data. Their qualities depend on the accuracy of the atmospheric correction algorithms. The approaches of the atmospheric correction for land and ocean are different due to the large difference of the ground reflectance between land and ocean. A unified atmospheric correction (UAC) approach is developed to improve the accuracy of aerosol products over land, similar to those over ocean. This approach is developed to estimate the aerosol scattering reflectance from satellite data based on a lookup table (LUT) of in situ measured ground reflectance. The results show that the aerosol scattering reflectance can be completely separated from the satellite measured radiance over turbid waters and lands. The accuracy is validated with the mean relative errors of 22.1%. The vertical structures of the aerosols provide a new insight into the role of aerosols in regulating Earth's weather, climate, and air quality.

Keywords: aerosol, epsilon, aerosol optical thickness, Angstrom exponent, atmospheric correction, land remote sensing, ocean colour remote sensing, the UAC model

1. Introduction

Aerosols, suspended particulate matter in air, act as a crucial factor in global climatic fluctuations [1]. Aerosols can affect the climate through absorption and scattering of solar radiation [2] and therefore perturb the radiation budget and contribute to radiative forcing [3]. Aerosols may change the size and density of cloud droplets, thus modify the cloud albedo, the cloud lifetime and the precipitation [4]. Aerosols also influence air quality and therefore affect human health [5]. Current uncertainties of aerosols in the Earth radiation budget limit our understanding of the climate system and the potential for global climate change [1]. Satellite observations are needed to understand the distribution and impact of aerosols on regional and global scales [6]. Satellites can monitor some aerosol optical properties, e.g. aerosol optical thickness (AOT) and Angstrom exponent, the key factors for climate change research [7]. In fact, these properties can be retrieved during the atmospheric correction of satellite images.

Ever since Gordon [8] designed an atmospheric correction approach based on the black ocean assumption (BOA) at two near-infrared (NIR) bands, this approach has been widely applied to process satellite ocean colour remote sensing data. The performance of the approach was improved significantly [9, 10]. However, this approach still faces problems in Case 2 waters [11]. Some other algorithms of atmospheric corrections have been developed especially for the coastal waters. These include the use of the assumption of spatial homogeneity of the NIR band ratio [12], the spectral shape matching methods [13], an iterative fitting algorithm with the bio-optical models [14], the BOA method using the short wave infrared (SWIR) bands over turbid waters [15] or the algorithm using the ultraviolet bands [16].

The atmospheric correction over land meets more complicated situations. Similar to the BOA approach for the ocean colour remote sensing, the dark target (DT) approach has been widely used to estimate the optical properties of aerosols over land [17]. Other approaches have been developed using different methods, for example, the invariant object approach by Hall et al. [18], the histogram matching by Richter [19] and the radiative transfer model by Gao et al. [20]. Traditionally, different approaches of the atmospheric correction are necessary for land and ocean to optimize each case. Recently, Mao et al. [21, 22] developed an approach to estimate the aerosol scattering reflectance over turbid waters based on a look-up table (LUT) of in situ measurements. Following this approach, a unified atmospheric correction (UAC) approach is developed for both land and ocean [23].

Over the last several decades, satellite remote sensing has provided an increasingly detailed view of aerosols and clouds [24] but limited with column-averaged aerosol properties. Aerosols in the lowest part of the atmosphere are likely to be removed quickly by the rain, those in higher altitudes are much more likely to travel long distances and affect air quality in distant regions. The Cloud-Aerosol Lidar and infrared pathfinder satellite observation (CALIPSO) satellite provides new capabilities to distinguish aerosol optically thin boundary layer from cloud by considering the vertical thickness and location of the layers as well as from the spectral behaviour of the lidar backscatter [25], useful in studying the interactions between aerosols and clouds with their roles in the climate system.

http://dx.doi.org/10.5772/65284

2. Methods

2.1. Retrieving the aerosols based on the BOA method

In the atmospheric correction procedure, the aerosol scattering reflectance needs to be estimated from remote sensing data, relying on the condition that it can be clearly separated from the total satellite-measured reflectance. This condition can be met using the BOA method over clear oceanic waters when the water-leaving reflectance in the NIR bands is negligible. The satellite-received reflectance at the TOA was defined by:

$$\rho_t(\lambda) = \pi L_t(\lambda) / (F_0(\lambda)\cos\theta_0) \tag{1}$$

where $L_t(\lambda)$ is the satellite-measured radiance, $F_0(\lambda)$ is the extra-terrestrial solar irradiance, and θ_0 is the solar-zenith angle. Wang [26] partitioned the term $\rho_t(\lambda)$ into components corresponding to distinct physical processes by:

$$\rho_t(\lambda) = \rho_r(\lambda) + \rho_A(\lambda) + t(\lambda)\rho_{wc}(\lambda) + T(\lambda)\rho_g(\lambda) + t(\lambda)\rho_w(\lambda) \tag{2}$$

where $\rho_r(\lambda)$ is the Rayleigh scattering reflectance due to the air molecules, $\rho_A(\lambda)$ is the aerosol scattering reflectance including the Rayleigh-aerosol interactions, $\rho_{wc}(\lambda)$ is the reflectance of the ocean whitecaps, $\rho_g(\lambda)$ is the reflectance of Sun glitter off the sea surface and $\rho_w(\lambda)$ is the water-leaving reflectance. The terms $t(\lambda)$ and $T(\lambda)$ are the diffuse and direct transmittances of the atmosphere, respectively.

$$\rho_A(\lambda) = \rho_t(\lambda) \text{-} \rho_r(\lambda) - T(\lambda)\rho_g(\lambda) - t(\lambda)\rho_{wc}(\lambda) - t(\lambda)\rho_w(\lambda) \tag{3}$$

When the water-leaving reflectance in the two NIR bands is assumed to be zero, the aerosol scattering reflectance can be obtained and used to compute the aerosol single scattering reflectance from:

$$\rho_{AS}(\lambda) = \frac{-b + \sqrt{b^2 - 4c(a - \rho_A(\lambda))}}{2c} \tag{4}$$

The epsilon spectrum of the aerosol single scattering reflectance is then defined as follows:

$$\varepsilon(\lambda_i, \lambda_0) = \frac{\rho_{AS}(\lambda_i)}{\rho_{AS}(\lambda_0)} \tag{5}$$

Angstrom exponent n is computed from:

$$n = \frac{\lambda_i}{\lambda_0} \cdot \varepsilon\left(\lambda_i, \lambda_0\right) \tag{6}$$

According to Ref. [27], the aerosol optical thickness (AOT) can be calculated from the aerosol single scattering reflectance as follows:

$$\tau_a(\lambda) = \rho_{AS}(\lambda) \Big/ \omega_a(\lambda) P_a(\lambda) \tag{7}$$

where $\omega_a(\lambda)$ is the aerosol single scattering albedo and $P_a(\lambda)$ is the aerosol scattering phase function.

2.2. Retrieving the aerosols based on the UAC model

The assumption of the BOA method becomes invalid over turbid waters and lands, leading to the failure of the standard atmospheric correction. A new approach needs to be developed to retrieve the aerosols from the satellite data. We define $\rho_{AW}(\lambda)$ as a term of the aerosol-water reflectance, which includes aerosol scattering reflectance and the ground reflectance at the top of the atmosphere (TOA), derived as follows.

$$\rho_{AW}(\lambda) = \rho_t(\lambda) \text{-} \rho_r(\lambda) - T(\lambda)\rho_g(\lambda) - t(\lambda)\rho_{wc}(\lambda) \tag{8}$$

Then, aerosol scattering reflectance $\rho_A(\lambda)$ can be obtained using:

$$\rho_A(\lambda) = \rho_{AW}(\lambda) - t(\lambda) \cdot \rho_w(\lambda) \tag{9}$$

It is derived from the normalized water-leaving reflectance, which is selected from a lookup table of the in situ measurements using the UAC method.

The epsilon spectrum is used to match the two closest aerosol models and obtain the corrected epsilon values $\varepsilon^c(\lambda_i, \lambda_0)$ following the approach of Mao et al. (2013). The Angstrom exponent $\eta(\lambda_i)$ is obtained from:

$$\eta\left(\lambda_i\right) = \ln(\varepsilon^c(\lambda_i, \lambda_0)) \cdot \lambda_0 / \lambda_i \tag{10}$$

We defined λ_M as a new reference wavelength obtained from the mean value of the band wavelengths.

$$\lambda_M = \sum \lambda_i / n \tag{11}$$

http://dx.doi.org/10.5772/65284

The corrected epsilon spectrum is adjusted by a new reference wavelength, defined as follows:

$$\varepsilon_M\left(\lambda_i,\lambda_M\right)=\left(\frac{\lambda_M}{\lambda_i}\right)^{\eta(\lambda_i)} \tag{12}$$

The aerosol single scattering reflectance is used to obtain the mean value, defined as follows:

$$\rho_{AS}(\lambda_M)=\sum\rho_{AS}(\lambda_i)/n \tag{13}$$

Then, a new aerosol single scattering reflectance is obtained from:

$$\rho^n{}_{AS}(\lambda_i)=\varepsilon_M\left(\lambda_i,\lambda_M\right)\cdot\rho_{AS}(\lambda_M) \tag{14}$$

This approach relies on the assumption that the aerosol scattering reflectance follows the Angstrom law instead of the BOA. This new assumption eliminates the effects of non-zero water-leaving reflectance in the atmospheric correction procedure. Due to the amplifying effects of the epsilon spectrum in estimating the aerosol scattering reflectance, the water-leaving reflectance may be estimated with large errors using the BOA method. One advantage of the UAC model is that the epsilon spectrum can be obtained to find the aerosol model, instead one value in the NIR band. The other advantage is that the difference of the ground reflectance among different objects is represented by different spectra in the LUT. Therefore, the LUT of the ground reflectance helps the UAC model to eliminate the different effects of the atmospheric correction due to the large difference of the reflectance between land and ocean.

2.3. Comparison between the UAC model and the BOA method

It is well known that the processing of satellite data using the standard atmospheric correction usually fails over turbid coastal regions. One of the main reasons is the difficulty in accurately determining the epsilon values. Epsilon is used to determine the magnitude of the aerosol scattering reflectance and deficiencies in its determination degrades the accuracy of the atmospheric correction of satellite remote sensing data. Normally, epsilon is estimated from aerosol scattering reflectance under the assumption of zero water-leaving radiance in the two NIR bands. However, the water-leaving radiance values in the two NIR bands are usually much higher than zero in the coastal waters [28], causing errors in the epsilon estimation.

This overestimation is caused by that the water-leaving reflectance is wrongly attributed as part of the aerosol scattering reflectance to overestimate the epsilon value. A small bias of the epsilon may easily lead to a relatively large error in the water-leaving reflectance due to the amplifying effects of the extrapolation of epsilon. The aerosol scattering reflectance obtained by the UAC model is different from that by the BOA method, especially in the coast regions.

A simple comparison is made based on three selected typical locations (marked by the green crosses in **Figure 3**), and the results are shown in **Figure 1**.

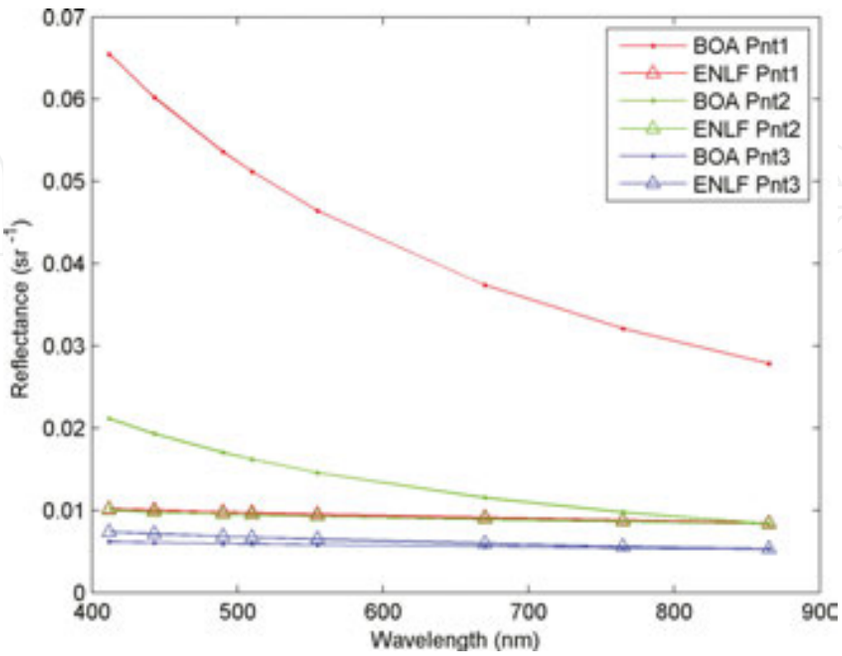

Figure 1. Comparison between the aerosol scattering reflectance using the UAC and the BOA method.

Epsilon	Band 1	Band 2	Band 3	Band 4	Band 5	Band 6	Band 7	Band 8
1–1.04	8.94	8.44	7.72	7.42	6.74	5.06	4.26	4.51
1.04–1.07	11.77	11.21	10.41	10.09	9.37	7.80	7.03	6.86
1.07–1.1	74.38	70.16	64.40	62.17	57.49	47.43	41.04	37.29
1.1–1.2	206.63	186.90	161.39	151.86	132.73	94.93	72.27	55.23
1.2–1.3	453.50	394.95	323.45	297.96	248.86	159.89	111.68	75.14
>1.3	961.04	796.23	612.95	552.07	441.02	259.90	172.08	110.42

Table 1. The difference between the aerosol reflectance obtained from the BOA method and that from the UAC model over the different epsilon ranges.

The aerosol scattering reflectance calculated from the two methods are similar to each other in oceanic waters (e.g. Location 3). The differences of the two reflectance spectra become larger near the coastal regions, with a mean relative error over 50% (e.g. Location 2). The difference of the two aerosol scattering reflectance values is very small in Band 8 and large in Band 1. This difference is attributed to the different epsilon values of the two methods, with 1.17 using the BOA method and 1.03 using the UAC model, respectively. A larger epsilon value will obviously overestimate the aerosol scattering reflectance, but this error is difficult to detect until a negative value of the water-leaving reflectance is produced. The BOA reflectance in Band 1 is

5.4 times larger than the UAC reflectance in highly turbid waters (e.g. Location 1). The value in Band 8 is also overestimated using the BOA method.

To evaluate the difference between the aerosol scattering reflectance using the two methods, the relative errors of the reflectance are computed according to the epsilon ranges (**Table 1**), in which the values using the UAC model are taken as the truth data.

From **Table 1**, the relative differences of the aerosol reflectance from the BOA method and the UAC model vary largely over the different epsilon ranges. The differences in all bands are relatively small for the epsilon value range of 1–1.07. The differences become higher than 50% for the range of 1.07–1.1. The differences become too much large when epsilon values are higher than 1.1, with a mean difference of 488% for the range of >1.3. Therefore, the BOA method is valid only with the epsilon value of less than 1.07.

A small error of the reflectance in NIR bands will cause somehow relatively larger error of the aerosol scattering reflectance using the BOA method. For example, two aerosol-water reflectance spectra are selected from two neighbouring pixels and shown in **Figure 2**, together with two aerosol scattering reflectance spectra obtained by the BOA method.

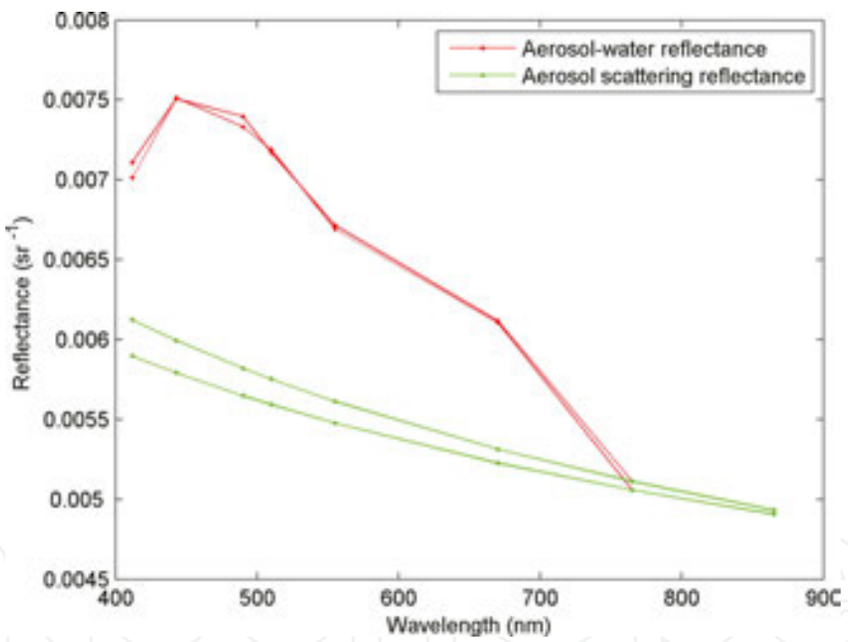

Figure 2. Comparison between the reflectance spectra at two neighbouring pixels. The red lines represent the aerosol-water reflectance from satellite data and the green lines are the aerosol scattering reflectance using the BOA method.

The magnitudes of the two aerosol-water reflectance are close to each other. But the differences of the reflectance in NIR bands lead to obtain two different epsilon values of 1.031 and 1.036 using the BOA method. Due to the amplifying effects, the difference in the two aerosol scattering reflectance is 2.26×10^{-4} sr^{-1} in Band 1, about 10-folds higher than that in Band 8. This difference tends to spread to the water-leaving reflectance in the atmospheric correction procedure with 2.1×10^{-4} sr^{-1} in Band 1, about threefolds of the difference between the satellite reflectance. The difference of the two aerosol scattering reflectance in Band 2 is up to 50-folds

higher than the satellite TOA values. Therefore, magnitudes of the aerosol scattering reflectance in the visible bands are very sensitive to the bias of the reflectance in the NIR bands using the BOA method. This problem can be significantly reduced by the UAC model.

3. Aerosols monitored by satellites over the ocean

3.1. Data

Aerosol robotic network (AERONET) is a ground-based optical aerosol monitoring network used to ensure the quality of aerosol products [29]. We obtained the AOT data from the AERONET project web page (http://aeronet.gsfc.nasa.gov). Data quality control is employed to eliminate errors caused by measurement conditions, such as clouds and biomass burning events [30]. There are a total of 554 measurement sites in the world. The site locations are distributed over islands, coastal areas, inland sites and mountains. The AOT was measured during the 2006 winter and 2007 autumn cruises over the ECS using a handheld multi-band sun photometer (MICROTOPS manufactured by the Solar Light Company). A total of 17 stations during the winter cruise, and 18 stations during the autumn cruise were measured with much more measurements during the transit between stations. To compare values between SeaWiFS and AOT, a matched data set was assembled using a time window for the satellite overpass of ±2 h from the in situ measurement. The locations of the matched dataset are shown in **Figure 3**.

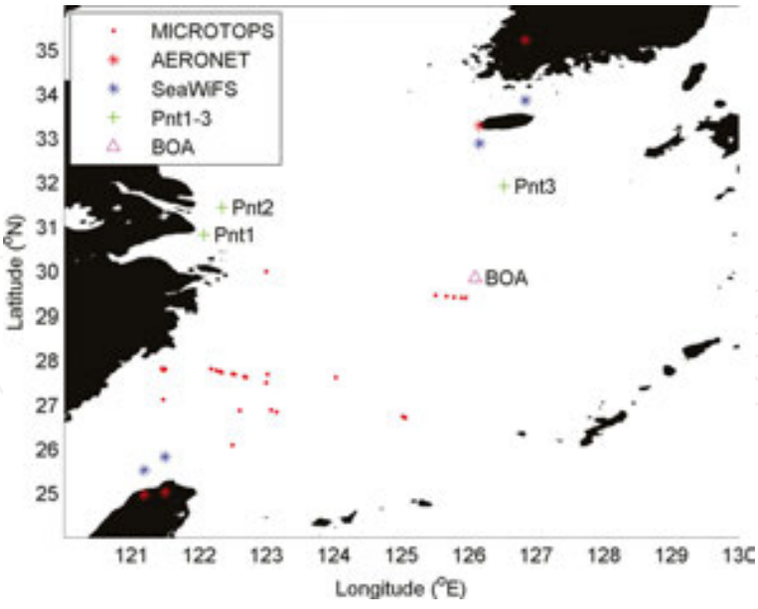

Figure 3. Some locations used in the paper. (1) Red dots represent the locations of matched MICROTOPS measured AOT and SeaWiFS data. (2) The three green crosses are the locations used for the comparison between the UAC model and BOA method. (3) The four blue stars are the locations of the AERONET sites and the nearby blue crosses are the locations for the matched SeaWiFS data. (4) The pink triangle is the location of the SeaWiFS measurements used for the analysis of the BOA method.

http://dx.doi.org/10.5772/65284

3.2. Some results

Normally, the accuracy of the aerosol scattering reflectance depends directly on the value of epsilon. A small error of the epsilon will easily lead to an amplified error in the aerosol scattering reflectance. If the entire epsilon spectrum instead of one value at the NIR band is used to determine the two closest aerosol models, the results are more robust. The key advantage of the UAC model is that it finds suitable aerosol models by matching the epsilon spectrum and thus improves the accuracy of the aerosol reflectance. The UAC model was used to process the SeaWiFS image on March 27, 2007 and the epsilon image is shown in **Figure 4**. To produce this image, the Rayleigh scattering reflectance was computed using a multiple scattering approach to obtain the aerosol-water reflectance. The aerosol scattering reflectance and the epsilon spectra were obtained by the UAC model.

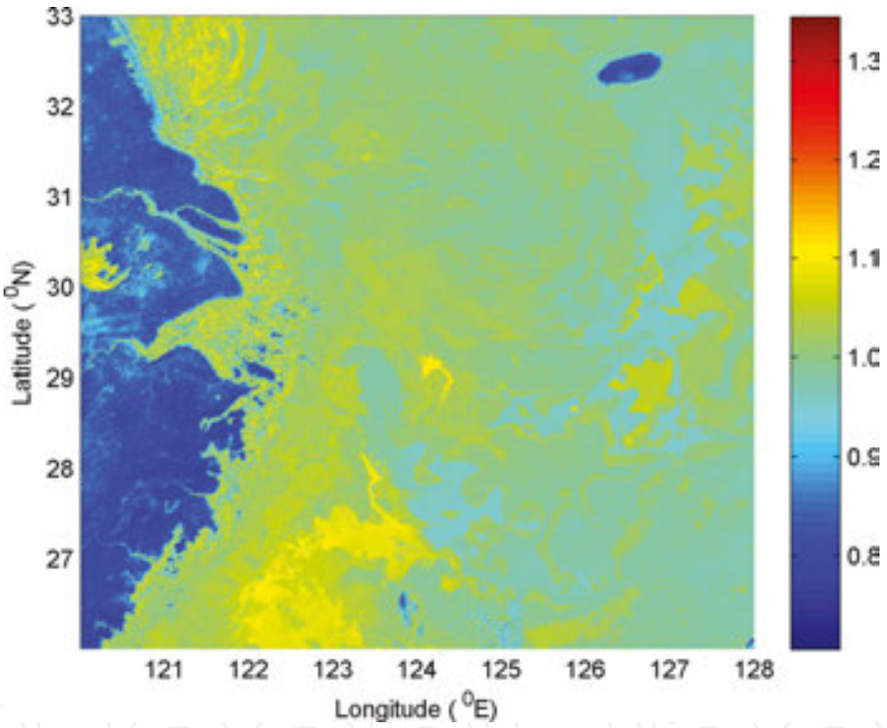

Figure 4. An epsilon image from SeaWiFS data on March 27, 2007 using the UAC model.

From the refined epsilon distribution in **Figure 4**, we can see that the high values of epsilon in the coastal regions are significantly reduced from around 1.4 to 1.05, with values closely in oceanic waters. As the spectra of the reflectance follow the Angstrom law, the structures of images in one band are similar to those in the other bands. The image of the aerosol scattering reflectance in Band 2 is selected and shown in **Figure 5**.

The $\rho_A(\lambda)$ values in Band 2 vary from 0.0042 to 0.015 sr^{-1}, with the mean value of 0.0092 sr^{-1} and the standard deviation of 0.0029 sr^{-1}. The distributions of the image indicate that $\rho_A(\lambda)$ varies significantly from one location to another, with the maxima in the northern part and the minima in the south. From the structures of the image in **Figure 5**, it is clear that the UAC

model has almost removed the influence effects of the non-zero water-leaving reflectance in the NIR bands in the coastal regions, even for highly turbid waters.

The water-leaving reflectance in the NIR bands varies from 0 to 0.06 sr^{-1}, almost six times higher than the aerosol reflectance. Under the BOA, up to six times extra values will be falsely added to the actual aerosol reflectance in the NIR bands, which obviously leads to the failure of the atmospheric correction procedure. In comparison, the UAC method makes use of the LUT, the magnitude variation in the ground reflectance has no effects in determining aerosol reflectance. The results show that the UAC model has clearly separated the aerosol scattering reflectance, working well from Case 1 to Case 2 waters.

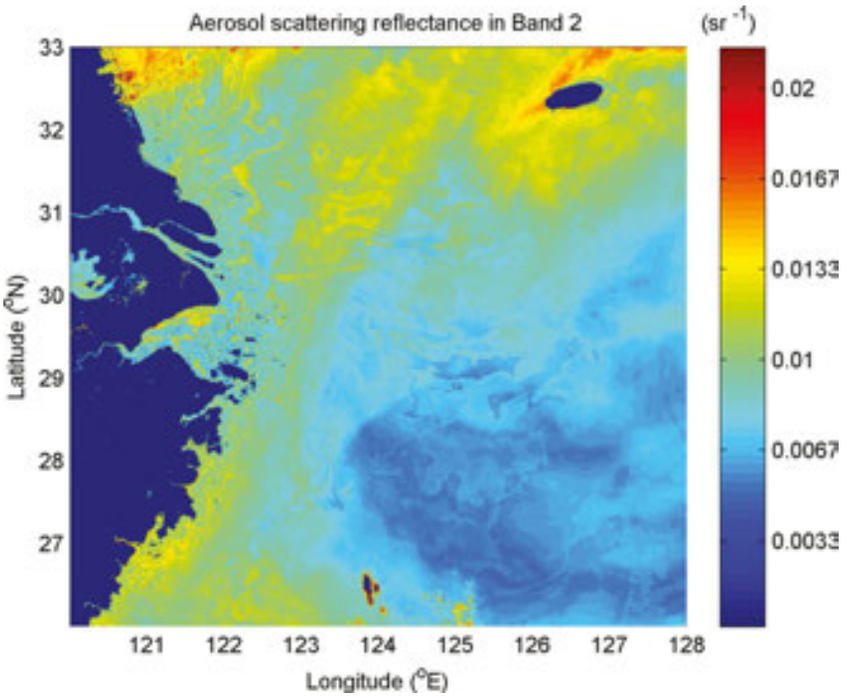

Figure 5. An image of aerosol reflectance retrieved from SeaWiFS Band 2 on March 27, 2007 using the UAC model.

3.3. Validation of the retrieval aerosols over the sea

The globally distributed AERONET data can be used to validate the aerosol products derived from satellite ocean colour remote sensing data such as SeaWiFS [31]. The SeaWiFS reflectance was processed to obtain epsilon using the UAC model, and the results are shown in **Figure 6**. The AOT spectra were used to calculate the aerosol reflectance using the geometric angles of SeaWiFS, to obtain the epsilon values.

Figure 6 shows that the two types of epsilon are relatively comparable. Both the magnitudes and the spectra shapes are similar to each other. AOT derived from MODIS and AERONET must be matched on space and time. Window size on space and time are set as 50 km × 50 km and 1 h in the anterior "http://www.iciba.com/" research. The correlation and regression coefficients show excellent agreement with AERONET measurements over the China Sea.

http://dx.doi.org/10.5772/65284

Meanwhile, the relationship is all good and their correlation coefficients are greater than 0.9. Errors of 65% points are under ± 0.05 ± 0.05 τ based on NASA standard. Fine mode fraction (FMF) is validated over the ocean with the error of about 20%.

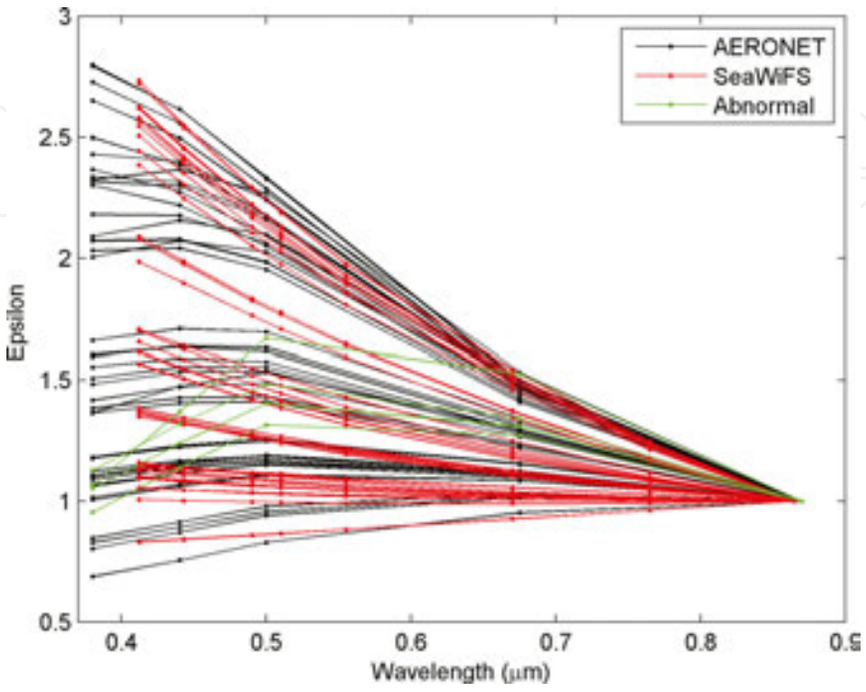

Figure 6. The comparison of the epsilon spectra from SeaWiFS reflectance using the UAC model (Red lines) to those from the AOT measured by the MICROTOPS instrument (Black lines) in the ECS. Green lines represent abnormal epsilon spectra.

Some factors affect the results of the validation. As the AOT data of AERONET are retrieved from the ground based radiance measurements, the data quality of AOT can also be affected by instrument calibration and the measurement conditions [30]. The translation from AOT to the aerosol scattering reflectance is related to the parameters of the aerosol single albedo and its phase function, which are determined by the absorption, and the type and particle size distribution of aerosols. These parameters were not measured, and typical values were used in the computation of epsilon from the AOT.

3.4. Spatial and temporal variations of aerosols over the ocean

The seasonal mean of MODIS AOT over the China Sea from 2001 to 2006, shown in **Figure 7**, demonstrates a notable seasonal change in spatial distribution. The maximum AOT appears in spring with the minimum in summer. In winter, high AOT is distributed along the coast and decreases obviously with the distance far from continent. Maximum AOT has been observed in coastal region and the value of it is larger than 0.5, meanwhile, the minimum AOT appears in open ocean and value of it is 0.1. The distribution of FMF is similar, suggesting that human activity influences aerosols. AOT over the north of 25°N is all larger than 0.17 and it over the south of 25°N is smaller than 0.17. The distribution of AOT in spring is similar to that

in winter. Because of dust prevailing, AOT increases obviously and is larger than 0.17 over the whole China Sea. The distribution in summer changes remarkably, with large values in the north and small in the south. Maxima appear over the Yellow Sea and Bohai Sea. Value of AOT in fall becomes the least in four seasons, and the pattern shows similarly structure of that in winter.

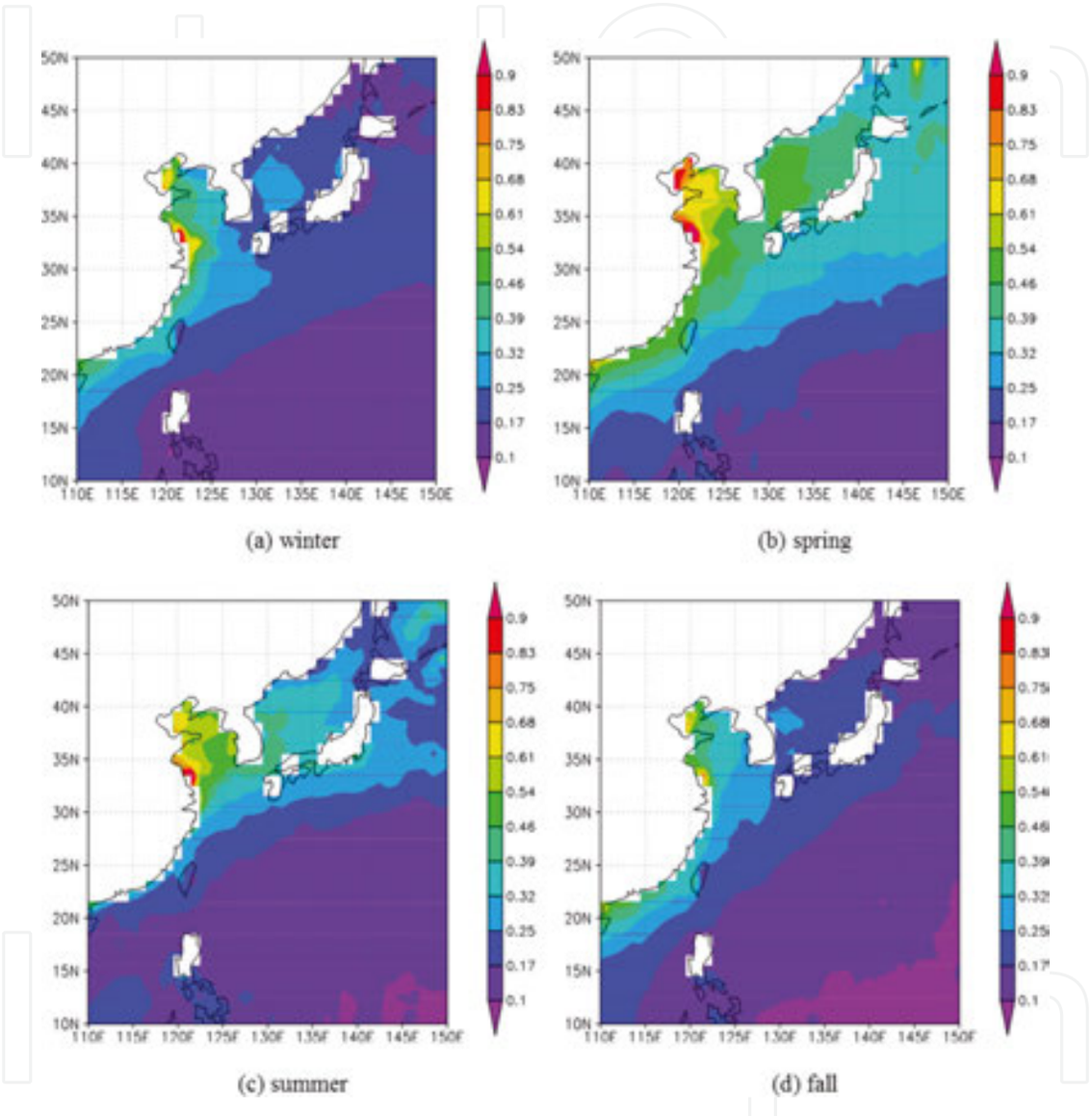

Figure 7. Seasonal distribution of AOT over the China Sea from 2001 to 2006. (a) winters; (b) spring; (c) summer; (d) fall.

Both AOT and FMF exist an annual cycle over the China Sea. The AOT appears maxima in spring with values larger than 0.4 and reaches minimum in summer with values less than 0.25. The FMF also has a periodic oscillation but an opposite tendency. The FMF reaches maxima in summer with values larger than 0.6 and gets minima in spring with values less than 0.5. The mean AOT and FMF during the 6 years (2001–2006) over the China Sea are shown in **Figure 8**. The AOT is the largest in April and the smallest in September, while the

http://dx.doi.org/10.5772/65284

FMF is the largest in September and the smallest in April. Based on the above analysis, we can find that AOT and FMF exist in significant temporal variety with an annual cycle over the China Sea.

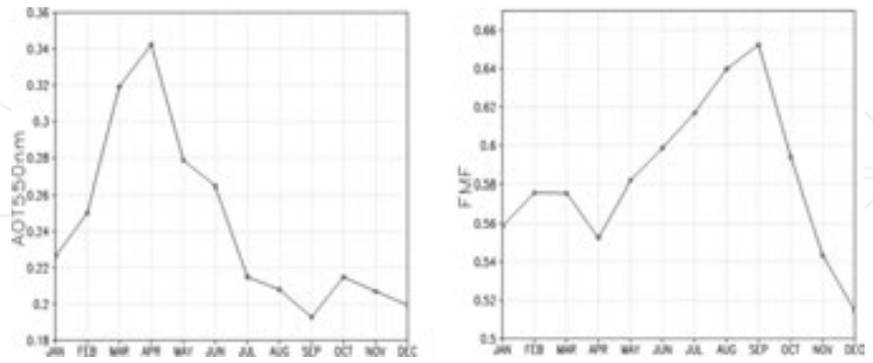

Figure 8. Monthly mean of the AOT (left panel) and the FMF (right panel) over the China Sea.

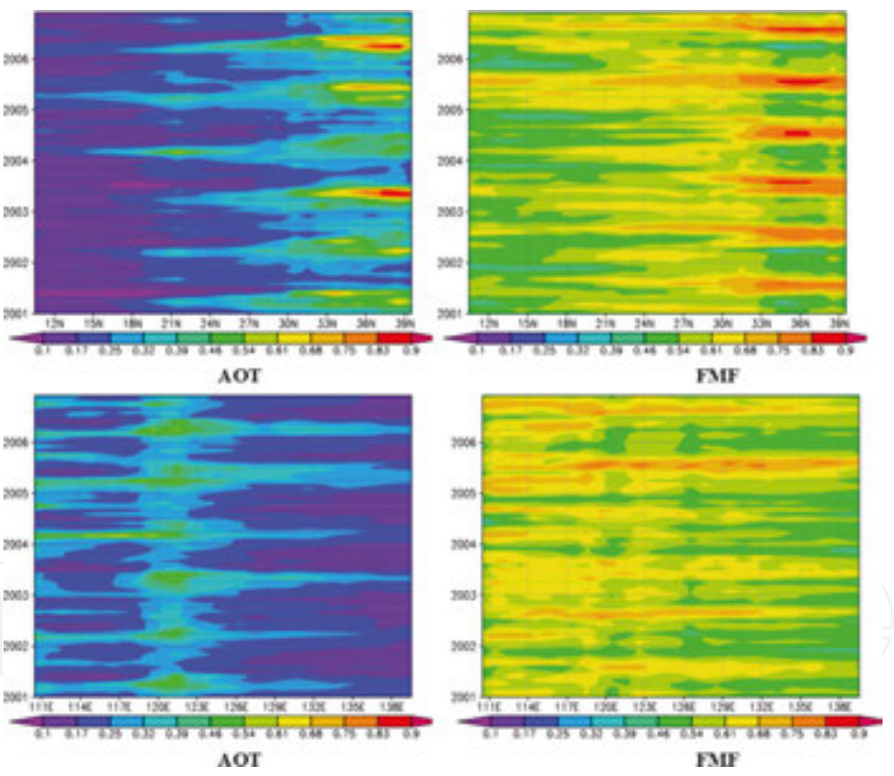

Figure 9. The latitudinal and longitudinal distribution of the AOT and FMF over the China Sea.

How about the spatial distribution of the AOT and FMF over the China Sea? The latitude-time and longitude-time diagrams of the AOT and FMF over the China Sea are shown in **Figure 9**. It represents a spatial characteristic related with the distance far from the coast and important industry regions, due to, which aerosols over the China Sea are mainly influenced by the continent source.

The AOT appears the highest value between 30°N and 40°N in the latitude direction, as there are main industry regions. The FMF also reaches the highest values in the same region. Both AOT and FMF get less towards the southern of the 30°N, due to lack of industry pollution. The human influence is very evident at longitude direction. China coast is around 120°E with the highest of the AOT and the FMF. Both the AOT and FMF gradually decrease away from the coast. The decrease tendency of AOT over the East China Sea has an affinity with the distance far from the continent, suggesting the AOT should be influenced by the continental sources.

3.5. Correlation to meteorological conditions

The aerosol's transport depends on wind, so seasonal change of wind may lead to the spatial and the temporal distribution of aerosols over the China Sea. The mean wind field at 850 hp in 2001–2006 is shown in **Figure 10**. The patterns are similar between winter and spring, demonstrating that northwestern wind control the north of 20°N and eastern wind control the south of 20°N. The eastern wind prevails at most of region in summer and fall, while south-western wind exists in the region between 30°N–40°N. Meanwhile, rainfall is the high in summer and low in winter and spring.

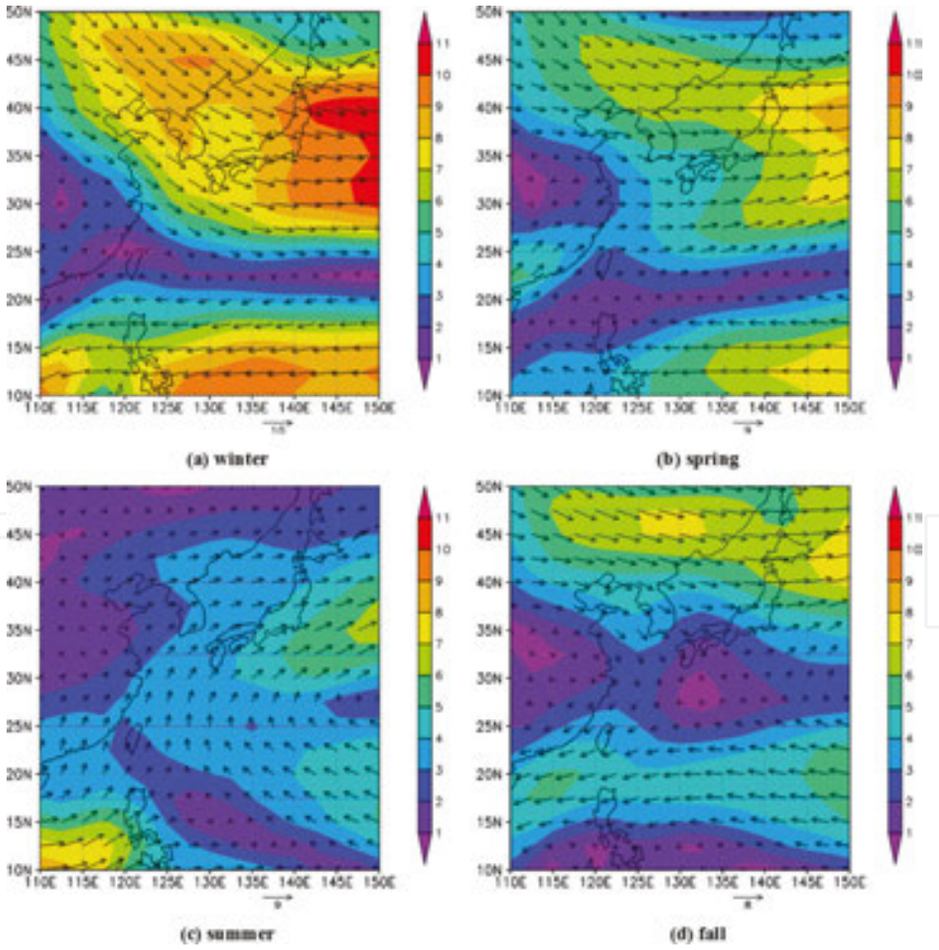

Figure 10. Seasonal distribution of wind field at 850 hp over the China Sea. (a) winters; (b) spring; (c) summer; (d) fall.

http://dx.doi.org/10.5772/65284

The aerosols are sent from the continental to ocean by the northwestern wind in winter. High wind speed causes that aerosol is difficult to bank up onto the China Sea, slowing down the values of the AOT. Meanwhile, high wind speeds create big particles of marine aerosol, leading to the smallest of the FMF. In spring, northwestern winds carry dust aerosols to the China Sea by and wind speed becomes weaker, so that aerosols build up onto the China Sea. The AOT reach maxima with a small of the FMF. In summer, east wind prevails, so continental aerosol can't be transported onto the sea. The rainfall is the large, bringing down the big particles of aerosols. So, the AOT is the smallest with the largest of the FMF. In fall, the west winds control the region of the north of 30° N, so the AOT is larger than summer. Rainfall is next below in summer, so the FMF is smaller than that in summer, but higher than that in other seasons. Therefore, meteorological conditions play an an important role on distribution of the AOT and FMF.

4. Aerosols monitored by satellites over the land

4.1. Data

Anhui province lies in the hinterland of Yangtze Delta in China between temperate zone and sub-tropical zone (**Figure 11**), one of the most important agricultural provinces covering 139,600 km^2. The agricultural activity and urbanization play important impacts on aerosols and air quality. For example, agricultural residues burning causes serious environment problem [32]. However, there is a little information related to aerosol characteristics with their influences of meteorological factors.

Figure 11. The geographical regions and the location of AERONET sites and meteorological stations.

One sample of SeaWiFS is selected and shown in **Figure 12**. It is a composite image of the satellite-received reflectance at the TOA on December 24, 2003. It covers a complicate structure

of the ground reflectance including very turbid waters to oceanic waters, showing a mixture of reflectance from the Rayleigh, aerosols, ocean and land.

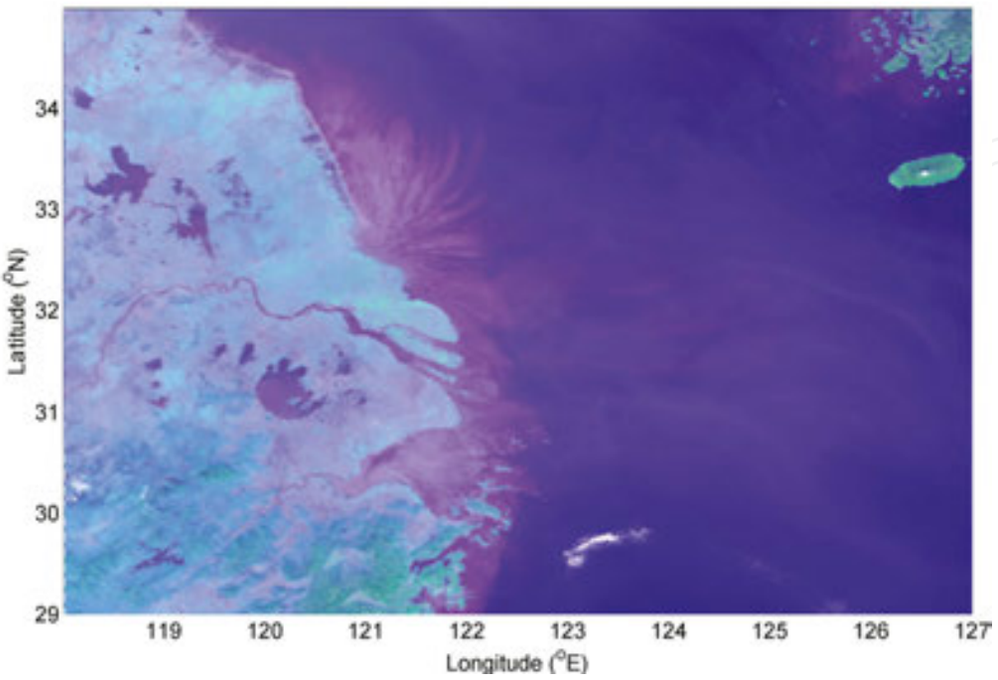

Figure 12. The image of the satellite-received reflectance at the TOA from SeaWiFS data on Dec. 24, 2003.

4.2. Some results

The UAC model uses the same computation method of the Rayleigh reflectance for the ocean and land, with the value is corrected by the elevation of the land surface. The aerosol reflectance obtained by the UAC model is shown in **Figure 13**, with significantly different structure from that of the ground reflectance. The image shows coherent spatial distributions extending from land into the coastal ocean, especially almost no difference in the aerosol distributions between lakes and nearby lands. The large spatial variations of the aerosol reflectance occur over the region around Shanghai and Lake Taihu. The spatial distribution of aerosols demonstrates that the UAC model has the advantage to estimate the aerosol reflectance without discontinuity between land and ocean.

4.3. Validating the retrieval aerosols over the land

There are more than 500 sites measured by AERONET around the world and four sites located in the region, which are EPA-NCU, Gosan_SNU, Gwangju_K-JIST and Taipei_CWB. The AOT data are used to obtain the aerosol scattering reflectance. They are matched with cloud free SeaWiFS data under the time difference of ±2 h at the same locations. The reflectance in Band 2 of the Gosan_SNU site is selected and shown in **Figure 14** according to the time of measurements.

http://dx.doi.org/10.5772/65284

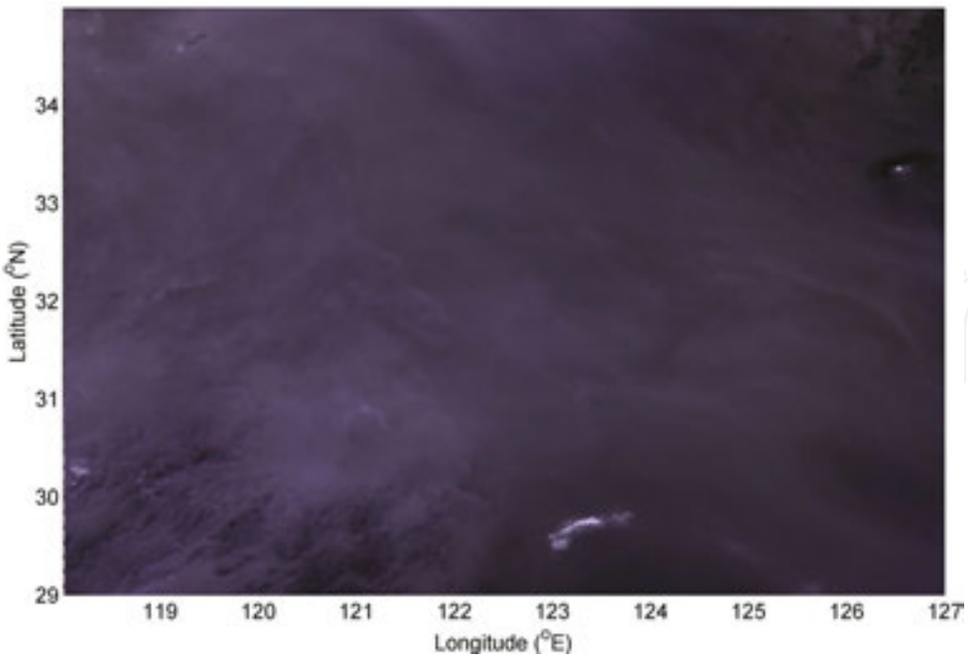

Figure 13. The aerosol reflectance obtained by the UAC model from SeaWiFS data on December. 24, 2003 shown with the RGB channels from Bands 6, 7 and 2.

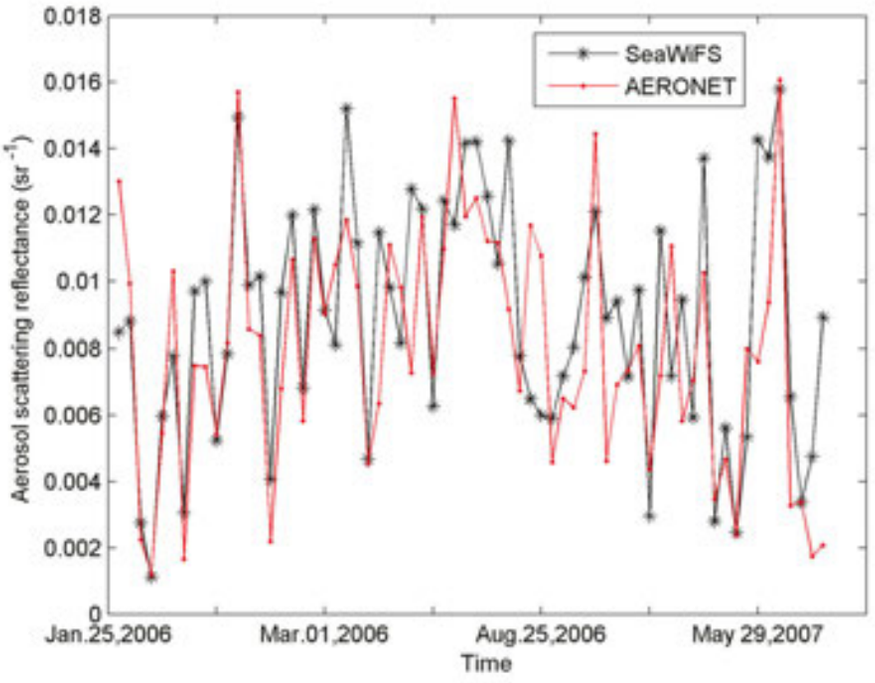

Figure 14. Comparison between the aerosol scattering reflectance from SeaWiFS data using the UAC model and that from the AERONET measurements in Band 2.

A total of 68 pairs of match-up data were established during 2006 and 2007 at the Gosan_SNU site. The aerosol scattering reflectance was obtained from SeaWiFS data using the UAC model and from the AOT data. The two reflectances in Band 2 vary consistently with each other, with the relative error of 21.9%. The reflectance in other four bands also displays similar results with the relative errors of 22.9, 23.8, 28.3 and 33.7%, respectively.

The aerosol scattering reflectance obtained from the AOT at other AERONET sites is also used to validate the accuracy of the reflectance from SeaWiFS data using the UAC model, shown in **Table 2**. Most of the relative errors are around 35%, with the mean values of 32.5, 33.3 and 33.6% corresponding to the sites of EPA-NCU, Gwangju_K-JIST and Taipei_CWB, respectively. The mean error of match-up pairs at the four sites is 31.4%. The standard deviations (STD) are almost the same, with only 2.8% difference. The two mean differences are the same, at 0.00085 sr^{-1}.

SeaWiFS (nm)	412	443	510	670	865
AERONET (nm)	380	440	500	675	865
Gosan_SNU (%)	22.88	21.94	23.84	28.29	33.74
EPA-NCU (%)	29.45	30.68	29.60	32.78	39.87
Gwangju_K-JIST (%)	28.30	28.51	30.62	36.14	43.16
Taipei CWB (%)	32.31	33.25	29.70	32.64	40.05

Table 2. The relative error of the SeaWiFS retrieval aerosol reflectance using the UAC model with respect to values calculated from the AERONET measured AOT data.

In order to take into account both spatial and temporal variations in aerosol distribution in Anhui, MODIS AOT at 10 km × 10 km resolution and AERONET AOT at 15-m intervals need to be co-located in space and time. In order to perform direct comparison and validation AOT at 550 nm, the values of AERONET AOT at 550 nm are retrieved by using Angstrom exponent calculated between 440 and 870 nm. The MODIS AOTs agree generally well with the AERONET AOTs. Most of dots overlay with the error range of $\triangle\tau = \pm 0.05 \pm 0.20\,\tau$. The linear fit slopes are less than 1, correlation coefficients are larger than 0.8, and RMS are less than 0.21 at four AERONET sites, which indicate that MODIS aerosol inversions have systematic biases in Anhui. The deviation from the unity of the slope of correlation plot represents systematic biases, whereas the intercept represents the errors due to surface reflectance assumptions [33]. The correlation coefficient results are all consistent.

4.4. Spatial and temporal variations of aerosols over the land

The spatial distribution and seasonal variations in AOT in Anhui averaged over the period 2001–2009 are presented in **Figure 15**. From the feature of aerosol spatial distribution, higher values of the AOT are observed in a large plain region at the north and middle of Anhui, while smaller values can been found over the mountainous region of southern Anhui centred over Huangshan and Dabieshan Mountain. We can find that the AOT is obviously influenced by

topography with lower AOT over the mountainous region. Big particle aerosols are removed by gravitational settling with dominant small particle aerosols when terrain altitudes increase. The AOT is higher over the plain region, due to complex aerosol sources from dust, industry emissions, biomass burning and traffic sources.

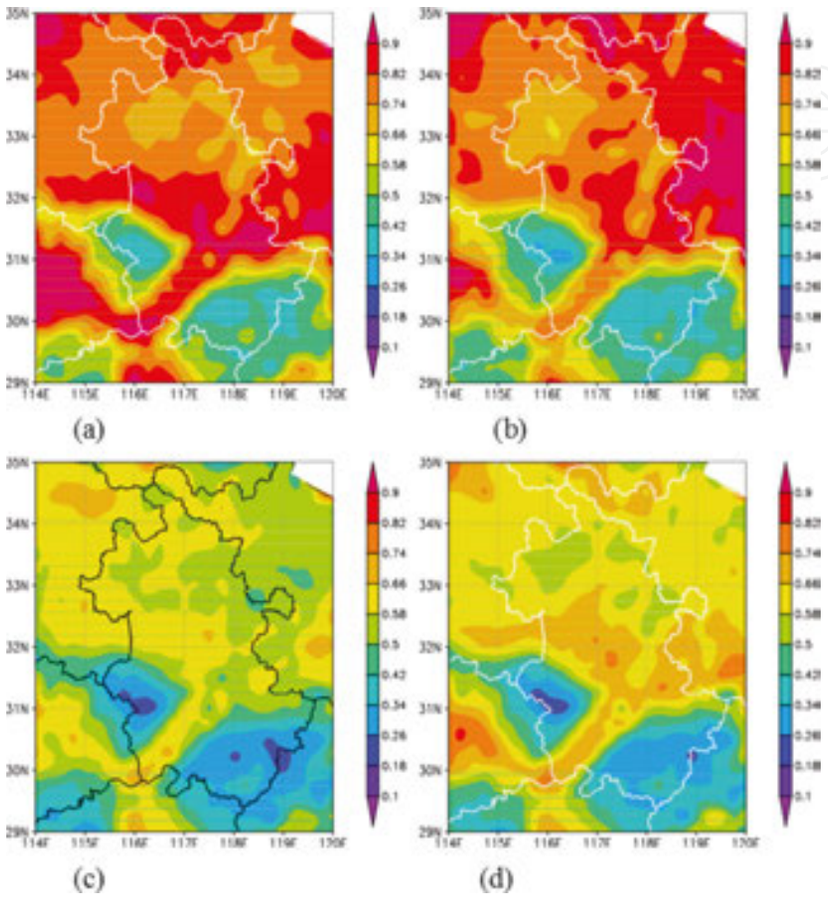

Figure 15. The seasonal mean of the AOT over Anhui province in China: (a) spring, (b) summer, (c) autumn and (d) winter.

The temporal variation of aerosol in Anhui can be well seen in **Figure 16**. It can be seen that there are obvious periodic variations in AOT, and the monthly variations are in agreement with the aforesaid result of seasonal changes. We find that the lowest AOT values are observed during the autumn with the highest during spring and summer. The high values of the aerosols are affected by dust originating from the northwestern China in spring. Despite that the amount of rainfall is maximum in summer, but the month of the highest AOT is June. The decrease in the AOT during autumn and winter is related with meteorological conditions.

4.5. The influence for aerosol by agricultural residues burning

The analysis shows that the month of the highest AOT is June. June is the beginning month of rainy season, in which AOT generally decreases by wet deposition. **Figure 17** shows a large increase (21%) in the AOT value from 0.77 in May to 0.93 in June and a prominent decrease

(32%) in AOT value from June (0.93) to July (0.63). The great change of AOT is likely from other sources of aerosols in June compared to in May and July. June is the time of agricultural residues burning after harvest periods in Anhui. Anhui province is a large agriculture area with about 30,000,000 tons of the grain output every year. The field burning is a general practice to clear the land for the next crop, controlling weeds and enriching soil nutrients. Thus, large amounts of aerosol particles are emitted by burning agricultural residues [34]. The fire pixels almost dominate the whole northern Anhui province and the fire pixel counts peak in June. Compared to the counts in other months, the fire pixel count is quite large in June and clearly matches with the high AOT loads during the burning month. As a result, the high AOT values observed in June in Anhui correspond to the burning agricultural.

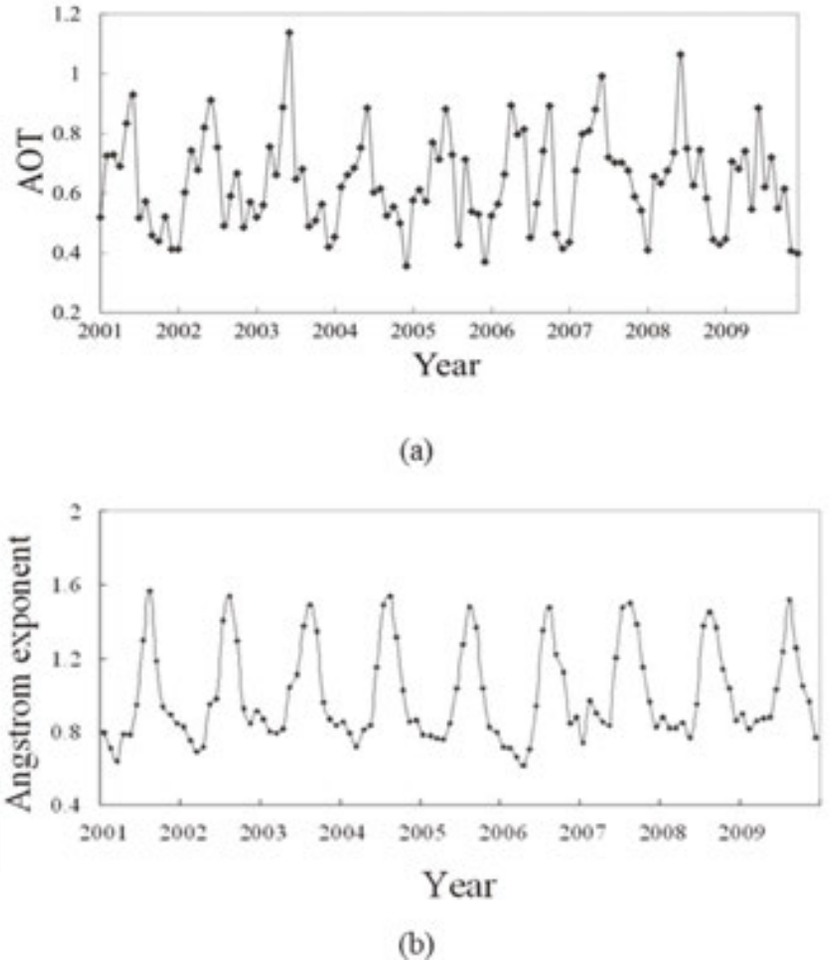

Figure 16. Monthly mean AOT and Angstrom exponent over Anhui province in China: (a) AOT and (b) Angstrom exponent.

4.6. Back trajectory analysis

The 3-day back trajectory analysis on 850 hPa was calculated to examine the aerosol sources of different AOT by using the hybrid single-particle Lagrangian integrated trajectory

http://dx.doi.org/10.5772/65284

(HYSPLIT) model. In order to obtain the influence for different aerosol particle size ranges by trajectories, two categories of back trajectories are defined based on values of the Angstrom exponent: coarse mode aerosol (CMA) with Angstrom exponent less than 1 and fine mode aerosol (FMA) with Angstrom exponent over 1, in order to obtain the influence for (**Figure 18**). A similar analysis for AOT degrees and the Angstrom exponent levels has been conducted.

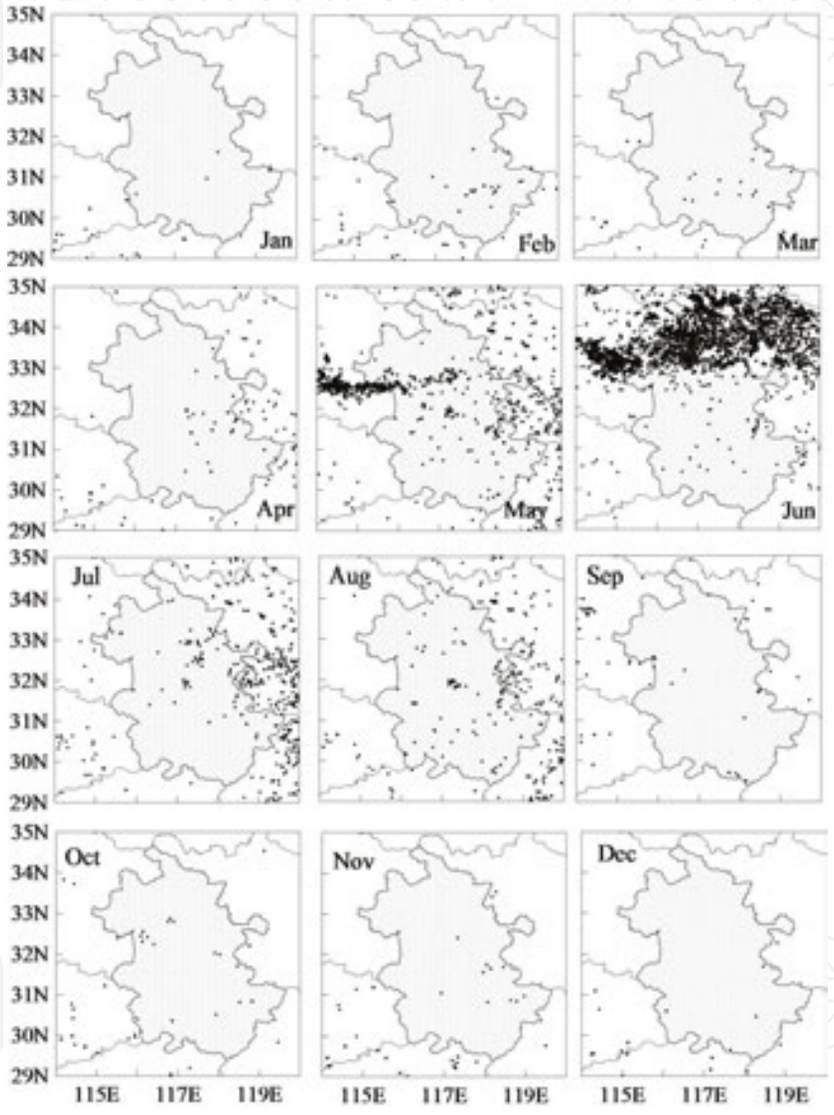

Figure 17. Monthly variation of fire pixels in 2007 in Anhui province from MODIS global monthly fire location product (MCD14ML). Fire pixels are shown in black dots.

For CMA category (**Figure 18a**), 8 clusters were obtained. The northwest transport pathway (Clusters 1, 2, 5–8) contributed 70% of all the trajectories, appearing with coarse mode aerosol. Long northwest clusters stand out with abundance of dusts, and dusts are carried by the northwest trajectories from dust sources to Fuyang. Therefore, aerosol particle sizes are mainly influenced by the northwest flows.

For FMA category (**Figure 18b**), six clusters were observed. Clusters 2 (13%) and 3 (8%) represent the northwest flows, while Cluster 1 represents the flow of the southwest sector (17%). Clusters 4 (23%), 5 (19%) and 6 (20%) have westerly, easterly and north easterly origins, respectively. The most notable difference of trajectories between CMA and FMA is the distance of transport flows. The long northwest trajectories (70%) are dominant for CMA, while the short transport flows (62%) are the most for FMA. This result is attributed to different aerosol types under different air masses. Therefore, anthropogenic aerosols mainly lead to fine mode, and natural aerosols dominate the long northwest trajectories.

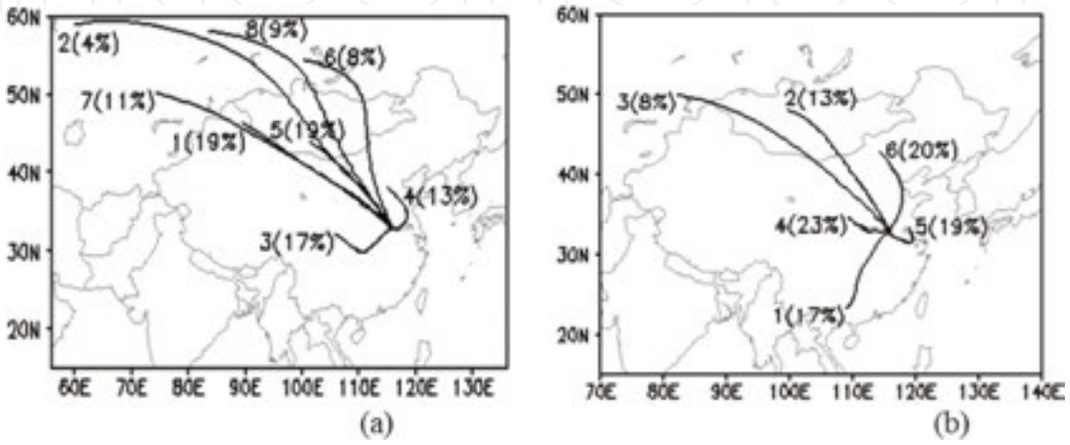

Figure 18. Mean HYSPLIT 72-h backward trajectories of 1500 m altitude at 02:30 GMT by cluster analysis during 2001–2009 at Fuyang station. (a) CMA, Angstrom exponent <1 and (b) FMA, Angstrom exponent > 1.

5. Aerosol vertical structures monitored by satellite lidar

5.1. Introduction

The CALIPSO combines an active lidar instrument with passive infrared and visible imagers to probe the vertical structure and properties of thin clouds and aerosols over the globe [35], to study the climate impact of clouds and aerosols in the atmosphere [36]. The Cloud-Aerosol Lidar with Orthogonal Polarization (CALIOP) is the primary instrument on the CALIPSO satellite, which is the first polarization lidar in orbit and the first satellite lidar [37]. It provides vertically resolved measurements of aerosol distribution with aerosol extinction coefficients [38] and observes aerosols over bright surfaces and beneath thin clouds as well as in clear sky conditions [39].

The CALIOP lidar consists of a laser and a receiver with the stability of the transmitter-to-receiver alignment [40]. The lasers produce simultaneous pulses at 532–1064 nm at a pulse repetition rate of 20.16 Hz, with a pulse length of about 20 ns. Polarization out-coupling provides a highly polarized beam with a beam diameter of 70 m at the Earth's surface [36]. A polarization beam splitter separates the 532 nm parallel and perpendicular returns. The receiver consists of the 1-m telescope and the photomultiplier tubes (PMTs).

The CALIOP acquires vertical profiles of elastic backscatter at two wavelengths from a near nadir-viewing geometry during both day and night phases of the orbit, to derive the accurate aerosol and cloud heights and extinction coefficient profiles. It measures the profiles of linear depolarization at 532 nm, to discriminate ice clouds from water clouds and to identify non-spherical aerosol particles [41]. The aerosol particle sizes can be obtained from the ratios of the signals obtained at the two wavelengths [42].

5.2. The algorithms to retrieve the aerosol vertical structures

The fundamental algorithms of the CALIPSO are profile processes, to locate all layer boundaries and to identify each layer as being either cloud or aerosol. There are three types of algorithms related with the layer detection, the feature classification and the optical properties analysis. The data products include layer heights (e.g. feature top and base altitudes), layer identification (i.e. clouds versus aerosols, ice clouds versus water clouds), layer structures of clouds, aerosol backscatter and extinction coefficients.

The first step is to identify the layer types of clouds and aerosols. Thus the layer detection algorithm is used to identify regions of enhanced scattering, and to record simple characteristics of these atmospheric features, and to detect the vertical location of several different classes of geophysical objects. Specifically, the lidar returns are used to obtain information on the base and top altitudes of clouds and aerosol layers [43]. The layer finding algorithm is based primarily on separating the genuine features from the pseudo-features to find layers repeatedly on several passes through the data. The distribution of the roughly separated aerosols with clouds is shown in **Figure 19**. The regions with white are recognized as clouds and the regions with yellow are taken as aerosols. The intensified backscattering values of clouds are centred at 1.5 km and those of aerosol layers are centred at 0.5 km.

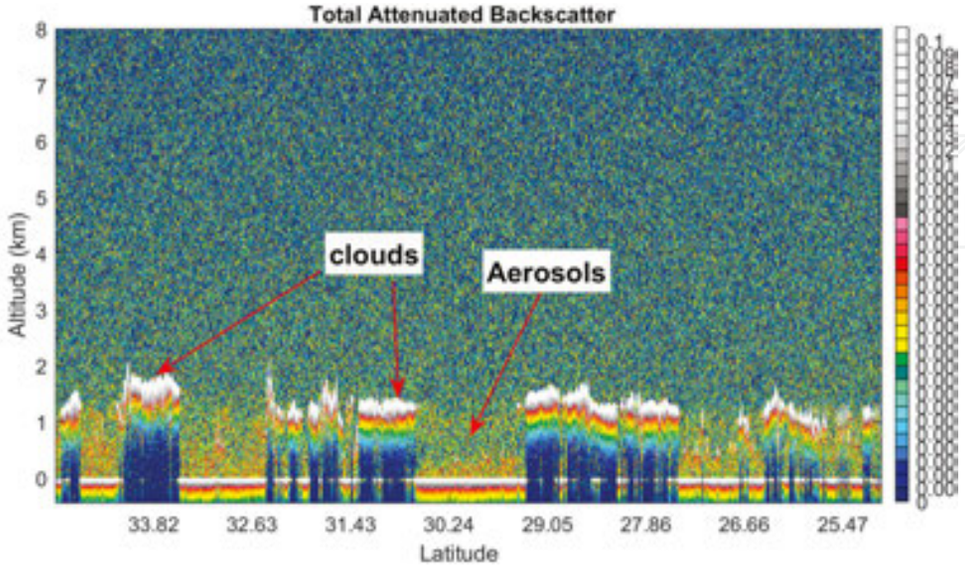

Figure 19. Aerosols and clouds can be roughly separated from the satellite data on Aug. 18, 2015.

5.3. Scene classification algorithm

The second processing step is to classify the layers and identify the types. The scene classification algorithm (SCA) is used to determine the types of the features (tropospheric or stratospheric) by checking the base altitude of the feature. The tropopause altitude is derived from ancillary data obtained from the global modelling and assimilation office and used to classify the tropospheric feature depending on whether the feature base is lower than this altitude, while the stratospheric feature is classified by that higher than this altitude. The further classification algorithms are conducted to sub-type the feature for the tropospheric feature.

The SCA is used to determine the aerosol layer or cloud layer, primarily based on the scattering strength and the spectral dependence of the lidar backscattering, which are primarily obtained from the mean value of the attenuated backscatter coefficient and the ratio of the mean attenuated backscatter coefficients (the attenuated colour ratio) at 1064–532 nm (**Figure 20**). If the layer is classified as cloud, the SCA will then determine whether it is an ice cloud or water cloud using the backscatter intensity and the depolarization ratio profiles together with ancillary information of the layer height and temperature. The SCA will also use a combination of observed parameters and a priori information to select an appropriate extinction-to-backscatter ratio and multiple scattering function required for subsequent process of the extinction and optical depth retrieve.

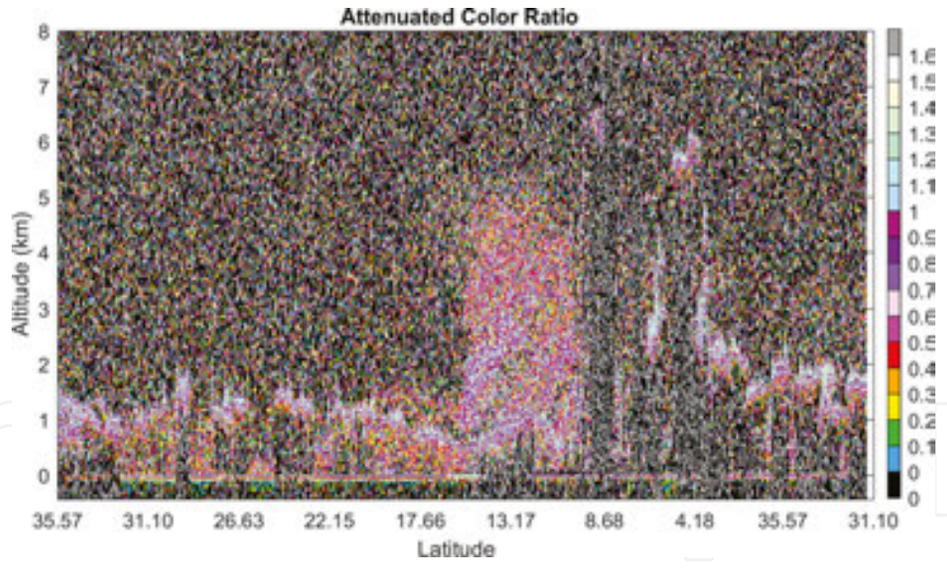

Figure 20. The attenuated colour ratio at 1064–532 nm for determining the layer type.

5.4. Retrieved optical properties analysis

The last processing step is to retrieve the extinction coefficient and optical depth from the calibrated, range-corrected lidar signal. Some widely used algorithms have been developed, based on the Fernald method [44], the Klett method [45] and the so-called linear iterative method [46]. The Fernald and Klett methods offer analytic solutions with closed form, while

http://dx.doi.org/10.5772/65284

the linear iterative technique is a simple numerical solution. Both Fernald and Klett methods are developed from the single scattering analyses to the multiple scattering analyses using a correction factor to the range-resolved extinction coefficients. The CALIPSO algorithms account for multiple scattering by applying a correction factor derived from the phase functions of aerosol models [47]. These methods are used to retrieve the extinction and backscatter profiles of cloud and aerosol layers.

After the layer profiles identified by layer detection algorithm and classified by the SCA, the hybrid extinction retrieval algorithm (HERA) performs extinction retrievals on regions of profile data [48]. HERA incorporates a sophisticated retrieval engine that extracts profiles of particulate backscatter and extinction coefficients from the profiles of attenuated backscatter coefficients identified as layers. One example of particulate backscatter and extinction at 532–1064 nm is shown in **Figure 21**. Following the retrieval of extinction profiles, other parameters can be computed by HERA, including optical depth, particle colour ratio and particle depolarization ratio [49].

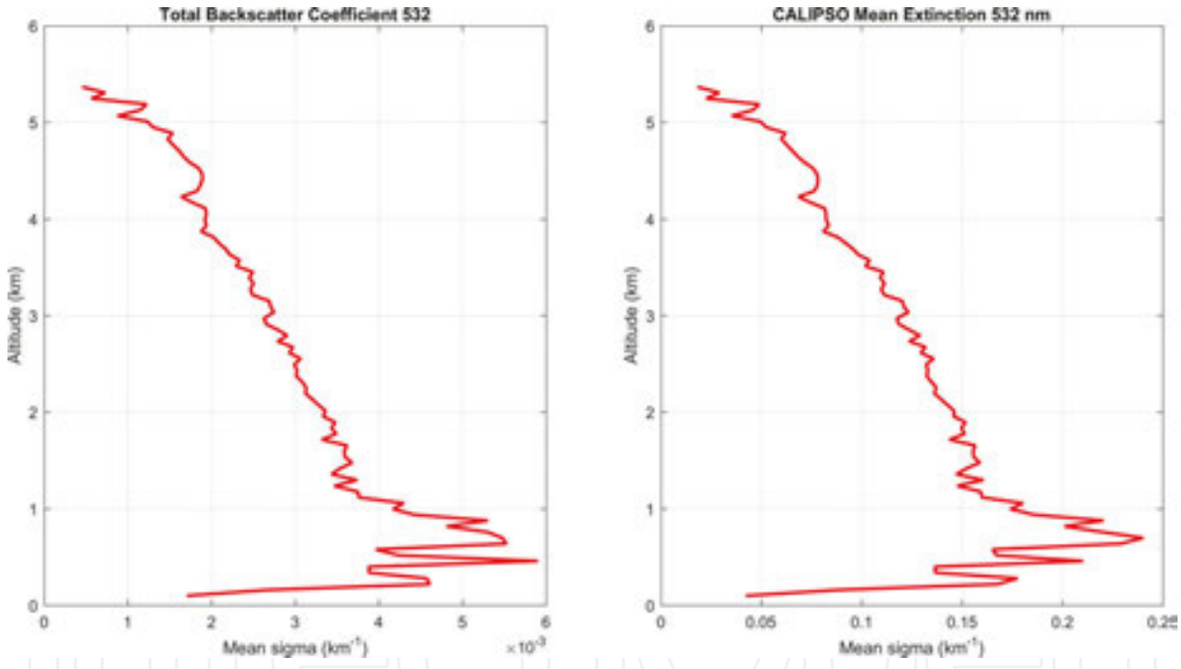

Figure 21. The left panel means profile of mean extinction at 532 nm; the right panel means profile of attenuation-corrected backscatter coefficient at 532 nm.

Column atmospheric optical depth can be estimated from the measured two-way transmittance at the ocean surface using ocean surface backscatter and collocated wind speed. Once the collocated wind speed is determined, theoretical ocean surface lidar backscatter can be derived from the wave slope variance—wind speed relation. The column optical depth is then derived from the ratio of the CALIPSO attenuated backscatter measurement and theoretical backscatter [50]. The cloud and aerosol optical depth derived from this approach is a direct measurement, without assuming aerosol and cloud physical properties. An example of aerosol optical depth distribution retrieved from CALIPSO data can be seen in **Figure 22**.

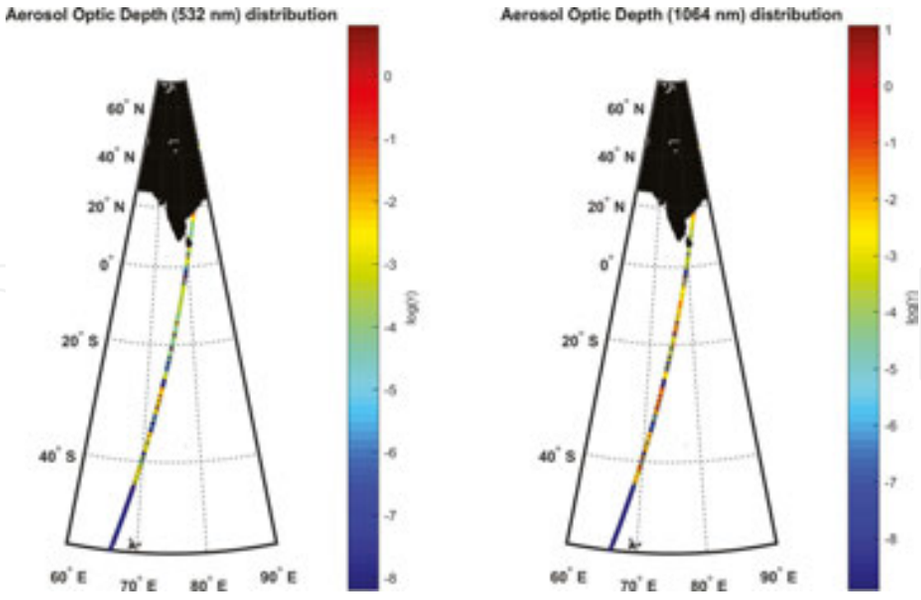

Figure 22. An example of AOD distribution retrieved from CALIPSO data with the AOD at 532 nm (the left panel) and 1064 nm (the right panel).

6. Conclusions

The ground reflectance is significantly different over land and ocean, leading to the need for different approaches of the atmospheric correction in order to optimize the results. However, this difference can be expressed by the spectra of the LUT of in situ measurements in the UAC model. Based on the LUT of the ground reflectance, the aerosol reflectance can be obtained by the best nonlinear least square fit function based on the Angstrom law. The reflectance is then used to determine the epsilon spectra that are used to select the two closest aerosol models instead of one epsilon value from the NIR band. The results show that this approach is more robust to overcome the problem caused by small variations in the aerosol reflectance in the two NIR bands. Meanwhile, this approach can also reduce some abnormal epsilon errors caused by factors including the data quality of satellite reflectance and the mismatch between the actual ground reflectance and the LUT. The use of the LUT provides a unified approach for estimating the aerosol reflectance and the ground reflectance over land and ocean. The performance of the UAC model is evaluated using a SeaWiFS image. The results show that the model can completely separate the aerosol scattering reflectance from the radiance at TOA. The relative error is 22.1% when it is validated by the in situ measured AOT data using the MICROTOP instruments, and the error is 31.4% using the four sites of AERONET measured AOT data over the ECS in 2006 and 2007. The UAC model can provide the aerosol products from satellite remote sensing data over land and ocean.

MODIS AOTs at 12 stations around China using the AERONET observations have been evaluated with the result that both agree generally well over ocean and land. The seasonal changes and spatial distributions of aerosol optical properties have also been observed with a notable

temporal variation over the China Sea. The AOT reaches maxima in spring and winter and minima in summer and fall, while the FMF reaches maxima in summer and fall and minima in spring and winter. Both AOT and FMF have an obvious spatial distribution over the China Sea. At latitude direction, the AOT appears maxima between 30 and 40°N and the FMF increases from south to north. At longitude direction, both AOT and FMF decrease with longitudinal increasing. Over the land, the lowest AOT values are observed during the autumn and the highest during the spring. The highest AOT, appearing in June, is possibly related to burning of agricultural residues. The Angstrom exponent appears maxima in summer and minima in winter. The higher AOT and lower Angstrom exponent are observed in a large plain region at the north and middle, while smaller AOT and higher Angstrom exponent can be found over the mountainous region, which is obviously influenced by topography. Meteorological conditions obviously affect the aerosol optical properties. Continent aerosol is carried to the China Sea by wind. The influences of different air masses are great disparity for aerosol optical properties over the land.

Acknowledgements

This study is supported by the National Key Research and Development Program of China (2016YFC1400901), the National Science Foundation of China (41476156, 41321004), and the Public Science and Technology Research Funds Projects of Ocean (201005030), the Anhui research project in the Public Interest (1604f0804003), and the China Special Fund for Meteorological Research in the Public Interest (GYHY201406039). We thank our colleagues from the Second Institute of Oceanography SOA, who took part in the cruises, for their hard work on in situ measurements. We also want to thank the experts who provided us their in-situ measurements.

Author details

Zhihua Mao[1,2*], Xueliang Deng[3], Peng Chen[1], Bangyi Tao[1], Guanying Yang[3], Yanfeng Huo[3] and Qiankun Zhu[1]

*Address all correspondence to: mao@sio.org.cn

1 State Key Laboratory of Satellite Ocean Environment Dynamics, Second Institute of Oceanography, State Oceanic Administration, Bochubeilu, Hangzhou, China

2 Nanjing University, Nanjing, China

3 Key Laboratory of Atmospheric Science and Satellite Remote Sensing, Anhui Institute of Meteorology, Hefei, China

References

[1] Griggs D J, Noguer M. Climate change 2001: The scientific basis. Contribution of Working Group I to the Third Assessment Report of the Intergovernmental Panel on Climate Change[J]. Weather, 2002, 57(8):267–269.

[2] Penner J E, Charlson R J, Schwartz S E, et al. Quantifying and minimizing uncertainty of climate forcing by anthropogenic aerosols. Bulletin of the American Meteorological Society, 1994, 75(3): 375–400.

[3] Satheesh S K, Moorthy K K. Radiative effects of natural aerosols: A review. Atmospheric Environment, 2005, 39(11): 2089–2110.

[4] Ramanathan V, Crutzen P J, Kiehl J T, et al. Aerosols, climate, and the hydrological cycle. Science, 2001, 294(5549): 2119–2124.

[5] Pope III C A, Burnett R T, Thun M J, et al. Lung cancer, cardiopulmonary mortality, and long-term exposure to fine particulate air pollution. JAMA, 2002, 287(9): 1132–1141.

[6] Winker D, Vaughan M, Hunt B. The CALIPSO mission and initial results from CALIOP[C]//Asia-Pacific Remote Sensing Symposium. International Society for Optics and Photonics, 2006: 640902–640902-8.

[7] Kaufman Y J, Tanré D, Boucher O. A satellite view of aerosols in the climate system. Nature, 2002, 419(6903): 215–223.

[8] Gordon H R. Removal of atmospheric effects from satellite imagery of the oceans. Applied Optics, 1978, 17(10): 1631–1636.

[9] Gordon H R, Brown J W, Evans R H. Exact Rayleigh scattering calculations for use with the Nimbus-7 Coastal Zone Color Scanner. Applied Optics, 1988, 27(5): 862–871.

[10] Ding K, Gordon H R. Analysis of the influence of O(2) A-band absorption on atmospheric correction of ocean-color imagery. Applied Optics, 1995, 34(12): 2068–2080.

[11] Wang M, Wei S. Estimation of ocean contribution at the MODIS near-infrared wavelengths along the east coast of the US: Two case studies[J]. Geophysical Research Letters, 2005, 32(13):370–370.

[12] Ruddick K G, Ovidio F, Rijkeboer M. Atmospheric correction of SeaWiFS imagery for turbid coastal and inland waters. Applied Optics, 2000, 39(6): 897–912.

[13] Shanmugam P, Ahn Y H. New atmospheric correction technique to retrieve the ocean colour from SeaWiFS imagery in complex coastal waters. Journal of Optics A: Pure and Applied Optics, 2007, 9(5): 511.

[14] Siegel D A, Wang M, Maritorena S, et al. Atmospheric correction of satellite ocean color imagery: The black pixel assumption. Applied Optics, 2000, 39(21): 3582–3591.

[15] Wang M. Remote sensing of the ocean contributions from ultraviolet to near-infrared using the shortwave infrared bands: Simulations. Applied Optics, 2007, 46(9): 1535–1547.

[16] He X, Bai Y, Pan D, et al. Using geostationary satellite ocean color data to map the diurnal dynamics of suspended particulate matter in coastal waters. Remote Sensing of Environment, 2013, 133: 225–239.

[17] Kaufman Y J, Sendra C. Algorithm for automatic atmospheric corrections to visible and near-IR satellite imagery. International Journal of Remote Sensing, 1988, 9(8): 1357–1381.

[18] Hall F G, Strebel D E, Nickeson J E, et al. Radiometric rectification: Toward a common radiometric response among multidate, multisensor images. Remote Sensing of Environment, 1991, 35(1): 11–27.

[19] Richter R. A spatially adaptive fast atmospheric correction algorithm. International Journal of Remote Sensing, 1996, 17(6): 1201–1214.

[20] Gao B C, Montes M J, Davis C O, et al. Atmospheric correction algorithms for hyperspectral remote sensing data of land and ocean. Remote Sensing of Environment, 2009, 113(9): S17–S24.

[21] Mao Z, Chen J, Hao Z, et al. A new approach to estimate the aerosol scattering ratios for the atmospheric correction of satellite remote sensing data in coastal regions. Remote Sensing of Environment, 2013, 132: 186–194.

[22] Mao Z, Pan D, Hao Z, et al. A potentially universal algorithm for estimating aerosol scattering reflectance from satellite remote sensing data. Remote Sensing of Environment, 2014, 142: 131–140.

[23] Mao Z, Pan D, He X, et al. A unified algorithm for the atmospheric correction of satellite remote sensing data over land and ocean. Remote Sense, 2016, 8: 536.

[24] King M D, Kaufman Y J, Tanré D, et al. Remote sensing of tropospheric aerosols from space: Past, present, and future. Bulletin of the American Meteorological Society, 1999, 80(11): 2229–2259.

[25] Winker D M, Pelon J, Coakley Jr J A, et al. The CALIPSO mission: A global 3D view of aerosols and clouds. Bulletin of the American Meteorological Society, 2010, 91(9): 1211.

[26] Wang M. Aerosol polarization effects on atmospheric correction and aerosol retrievals in ocean color remote sensing. Applied Optics, 2006, 45(35): 8951–8963.

[27] Gordon H R, Castaño D J. Aerosol analysis with the coastal zone color scanner: A simple method for including multiple scattering effects. Applied Optics, 1989, 28(7): 1320–1326.

[28] Mao Z, Chen J, Pan D, et al. A regional remote sensing algorithm for total suspended matter in the East China Sea. Remote Sensing of Environment, 2012, 124: 819–831.

[29] Holben B N, Eck T F, Slutsker I, et al. AERONET—A federated instrument network and data archive for aerosol characterization. Remote Sensing of Environment, 1998, 66(1): 1–16.

[30] Smirnov A, Holben B N, Eck T F, et al. Cloud-screening and quality control algorithms for the AERONET database. Remote Sensing of Environment, 2000, 73(3): 337–349.

[31] Mélin F, Vantrepotte V. How optically diverse is the coastal ocean. Remote Sensing of Environment, 2015, 160: 235–251.

[32] He L M, Wang W J, Wang Q, et al. Evaluation of the agricultural residues burning reduction in China using MODIS fire product. Environmental Monitoring in China, 2007, 23(1): 42–50.

[33] Remer L A, Kaufman Y J, Tanré D, et al. The MODIS aerosol algorithm, products, and validation. Journal of the Atmospheric Sciences, 2005, 62(4): 947–973.

[34] Zhang H, Ye X, Cheng T, et al. A laboratory study of agricultural crop residue combustion in China: Emission factors and emission inventory. Atmospheric Environment, 2008, 42(36): 8432–8441.

[35] Sassen K, Wang Z, Liu D. Global distribution of cirrus clouds from CloudSat/Cloud-Aerosol Lidar and Infrared Pathfinder Satellite Observations (CALIPSO) measurements[J]. Journal of Geophysical Research Atmospheres, 2008, 113(8):347–348.

[36] Lu X, Hu Y, Trepte C, et al. Ocean subsurface studies with the CALIPSO space borne lidar. Journal of Geophysical Research: Oceans, 2014, 119(7): 4305–4317.

[37] Winker D M, Hostetler C A, Vaughan M A, et al. CALIOP algorithm theoretical basis document, part 1: CALIOP instrument, and algorithms overview. Release, 2006, 2: 29.

[38] Liu D, Wang Z, Liu Z, et al. A height resolved global view of dust aerosols from the first year CALIPSO lidar measurements[J]. Journal of Geophysical Research Atmospheres, 2008, 113(D16):280–288.

[39] Geng F, Liu Q, Chen Y, et al. Preliminary study of vertical distribution of aerosols during dry haze periods around Shanghai based on CALIPSO. Procedia Earth & Planetary Science, 2011, 2(1): 217–222.

[40] Winker D M, Vaughan M A, Omar A, et al. Overview of the CALIPSO mission and CALIOP data processing algorithms. Journal of Atmospheric and Oceanic Technology, 2009, 26(11): 2310–2323.

[41] Winker D M, Hunt W H, Mcgill M J. Initial performance assessment of CALIOP[J]. Geophysical Research Letters, 2007, 34(19):228–262.

[42] Lindberg J D, Loveland R B, Duncan L D, et al. Vertical Profiles of Extinction and Particle Size Distribution Measurements Made in European Wintertime Fog and Haze[J]. ASL-TR-0151, 1984,1: 88002.

[43] Mark A. Vaughan, David M. Winker, Kathleen A. Powell, et al. Fully automated analysis of space-based lidar data: an overview of the CALIPSO retrieval algorithms and data products[J]. Proceedings of SPIE - The International Society for Optical Engineering, 2004, 5575:16–30.

[44] Fernald F G. Analysis of atmospheric lidar observations: Some comments. Applied Optics, 1984, 23(5): 652–653.

[45] Klett J D. Lidar inversion with variable backscatter/extinction ratios. Applied Optics, 1985, 24(11): 1638–1643.

[46] Elterman L. Aerosol measurements in the troposphere and stratosphere. Applied Optics, 1966, 5(11): 1769–1776.

[47] Omar A H, Winker D M, Won J G. Aerosol models for the CALIPSO lidar inversion algorithms[C]//Remote Sensing. International Society for Optics and Photonics, 2004, 1: 153–164.

[48] Vaughan M A, Winker D M, Hostetler C A. SIBYL: a selective iterated boundary location algorithm for finding cloud and aerosol layers in CALIPSO lidardata[J]. Lidar Remote Sensing in Atmospheric and Earth Sciences, 2002, 1: 791–794.

[49] Young S A, Winker D M, Vaughan M A, et al. CALIOP algorithm theoretical basis document, part 4: Extinction retrieval algorithms[J]. NASA Langley Research Center, Tech. Rep, Hampton, Virginia, 2008.

[50] Hu Y. Ocean, Land and Meteorology Studies Using Space-Based Lidar Measurements[C]. Proceedings of the 5th WSEAS International Conference on REMOTE SENSING,2009,1:47–50.

IntechOpen